THE JOURNAL OF
PHYSICAL CHEMISTRY B

Article

pubs.acs.org/JPCB

Detection of CuAuPd Phase Boundaries Using Core Level Shifts

Chunrong Yin,[†] James B. Miller,[†] Petro Kondratyuk,[†] and Andrew J. Gellman*[,†,‡]

[†]Department of Chemical Engineering and [‡]W.E. Scott Institute for Energy Innovation, Carnegie Mellon University, Pittsburgh, Pennsylvania 15213, United States

ABSTRACT: A high throughput study has been conducted of the Cu $2p_{3/2}$, Au $4f_{7/2}$, and Pd $3d_{3/2}$ X-ray photoemission spectra obtained from a continuous distribution of $Cu_xAu_yPd_{1-x-y}$ alloy samples prepared as a single composition spread alloy film (CSAF). All three elements exhibit shifts of their core level binding energies with respect to their pure states when diluted into the alloy. The Cu $2p_{3/2}$ core level shift (CLS) exhibits additional shifts over the composition ranges at which the $Cu_xAu_yPd_{1-x-y}$ alloy transitions between FCC and B2 phases. This discontinuous CLS has been used to map the extent of the B2 phase across the ternary $Cu_xAu_yPd_{1-x-y}$ alloy composition space. The sensitivity of core level binding energies to the alloy phase offers an opportunity to use XPS to study phases in alloy nanoparticles, ultrathin films, and other morphologies that are not amenable to structure determination by diffraction based methods.

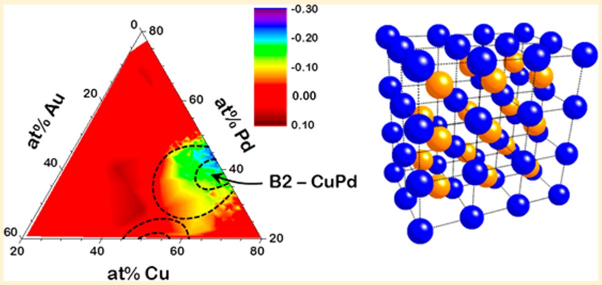

1. INTRODUCTION

Understanding of phase diagrams is core to the materials science of multicomponent mixtures such as alloys. This is just as true for materials in novel morphologies such as thin films and nanoparticles as it is for bulk materials. Recent work has shown that there are interesting examples of alloy compositions at which the phases that are stable at the nanoscale are not the same as those that are most stable in the bulk.[1−3] This observation opens an avenue to development of new materials with properties at the nanoscale that could not be predicted on the basis of those of the bulk. Pursuing this opportunity requires methods for identifying phases and finding phase boundaries in alloy materials with morphologies that are not amenable to phase determination with traditional diffraction based methods. Herein, we demonstrate the use of X-ray photoemission core level binding energies to map phases and their boundaries in a $Cu_xAu_yPd_{1-x-y}$ alloy thin film with compositions that span the entire ternary alloy composition space; $x = 0 \to 1$, $y = 0 \to 1 - x$.

Interest in Pd alloys arises from the fact that they are used for a wide variety of purposes, some of which require nanoscale morphologies. Thin membranes of Pd alloys are used for hydrogen purification from mixed gas streams.[4] Pd is used for its resistance to oxidation and for its high H atom permeability. Alloying Pd with components such as Cu, Ag, and Au is also known to increase mechanical strength and provide resistance to contamination by sulfur containing compounds.[5−7] In nanoparticulate form, Pd alloys are used as catalysts for reactions such as acetylene hydrogenation,[8] reduction of nitrates and nitrites,[9,10] catalytic combustion of methane[11] and as auto exhaust catalysts.[12] In these types of applications, the alloy phase can be an important determinant of its functional properties. For example, at temperatures <900 K, Cu_xPd_{1-x} alloys with compositions in the range $x = 0.50{-}0.65$ adopt the B2 structure rather than the FCC structure found for pure Cu and Pd.[13,14] This B2 phase has atoms on a BCC lattice and is lower in density than the FCC phase. As a consequence, its H atom permeability is almost an order of magnitude greater than that of the FCC Cu_xPd_{1-x} alloy.[15] Equally interestingly, the rate of catalytic H_2 dissociation on the alloy surface is much higher on $Cu_{0.53}Pd_{0.47}$ in its FCC phase than in the B2 phase.[16]

The bulk phase diagram for the $Cu_xAu_yPd_{1-x-y}$ ternary alloy system is well understood and is illustrated at 820 K in Figure 1.[17] At temperatures >900 K, the alloy forms a random solid solution on an FCC lattice. At 820 K, several phase boundaries have formed. As mentioned, a B2 phase exists along the CuPd binary line. As shown by the graphic illustration in Figure 1, the B2 CuPd alloy has a CsCl structure which is an ordered BCC lattice with Cu atoms at the centers of the unit cells and Pd atoms at the vertices. The B2 phase extends into the ternary composition space of $Cu_xAu_yPd_{1-x-y}$ to a maximum Au content of ∼10 at.%. The pure B2 region is surrounded by a B2 + FCC two-phase region that extends to ∼20 at.% Au. At compositions around $Cu_{0.50}Au_{0.30}Pd_{0.20}$, a third phase is formed which has the $L1_0$ CuAu structure consisting of layers of Cu atoms separated by layers of mixed AuPd. This single phase region is surrounded by a two-phase region. Mapping such a complex phase diagram requires preparation and structural characterization of alloy samples with compositions that sample the entire composition space.

In this work, we use the Cu $2p_{3/2}$ core level binding energy, measured using X-ray photoemission spectroscopy (XPS), as a means of mapping the B2 phase across $Cu_xAu_yPd_{1-x-y}$

Special Issue: Miquel B. Salmeron Festschrift

Received: July 6, 2017
Revised: September 14, 2017
Published: September 15, 2017

DOI: 10.1021/acs.jpcb.7b06652
J. Phys. Chem. B 2018, 122, 764−769

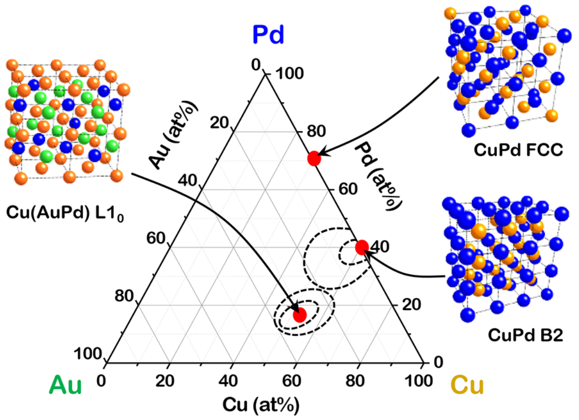

Figure 1. CuAuPd ternary phase diagram at 820 K.[17] Most of the composition space contains a random solid solution phase on an FCC lattice. This structure is illustrated by the inset at the top right for the CuPd alloy at ~70 at. % Pd. At ~40 at. % Pd, the CuPd alloy has an ordered B2 phase illustrated with its ideal BCC-like, CsCl structure having one Cu and one Pd atom per unit cell. Also shown at $Cu_{0.50}Au_{0.30}Pd_{0.20}$ is the L1$_0$ AuCu structure with layers of Cu atoms separated by layers of mixed AuPd.

composition space. Earlier work has shown that, in Cu_xPd_{1-x} binary alloys, the Cu 2p$_{3/2}$ core level binding energy decreases as the Cu content decreases.[18,19] In the FCC alloy, the core level shift (CLS) is monotonic. For Cu_xPd_{1-x} annealed at 800 K, we have demonstrated that the CLS is nonmonotonic and exhibits discontinuous shifts across the boundaries between FCC and B2 phases. Computational modeling has indicated that the discontinuous change in CLS arises from the discontinuous change across the phase boundaries of the average number of Cu−Cu nearest neighbors.[20] The FCC phase is a random solid solution of Cu and Pd, and the average number of Cu atoms in the nearest neighbor shell of a Cu atom is a smooth function of the Cu concentration. In contrast, the ideal B2 phase of $Cu_{0.50}Pd_{0.50}$ is an ordered structure in which there are no Cu atoms in the nearest neighbor shell of a Cu atom (see Figure 1). If the Cu 2p$_{3/2}$ CLS is dictated by Cu−Cu nearest-neighbor interactions, then it will change discontinuously across the FCC−B2 phase boundaries. In reality, of course, the transition from one value to another will be mitigated by the presence of a two-phase region between the FCC and B2 phases. One of the potential values of XPS, as a method for phase determination, is that it does not require the long-range order needed for structure determination using diffraction based techniques. Thus, in principle, XPS can be used to study the structures of material morphologies such as nanoparticulate phases that are not amenable to determination by X-ray diffraction.

In this work, we develop and demonstrate a high throughput method that can map ternary alloy phases across composition space in one experiment using spatially resolved X-ray photoemission spectra mapped across a composition spread alloy film (CSAF) library. The $Cu_xAu_yPd_{1-x-y}$ CSAF is a materials library in the form of a thin (<100 nm thick) alloy film deposited on a 14 × 14 mm^2 substrate in such a way that there is a triangular region with pure Cu, Au, and Pd at the vertices and all possible ternary compositions in the interior. Consistent with our understanding of the origin of the Cu 2p$_{3/2}$ CLS, we demonstrate that the CSAF can be used for high throughput mapping of the composition range of the B2 phase but not the L1$_0$ phase.

2. EXPERIMENTAL SECTION

2.1. Preparation of the CuAuPd CSAF.

CSAFs are multicomponent material libraries prepared as thin films deposited onto substrates such that there is a continuous composition distribution lateral to the substrate surface. Our $Cu_xAu_yPd_{1-x-y}$ CSAFs were designed to span the entire alloy composition space such that $x = 0 \rightarrow 1$ and $y = 0 \rightarrow 1 - x$. The library is deposited in the form of a triangle such that the vertices contain only the pure components and the three edges contain only the binary alloys Cu_xPd_{1-x}, Au_xPd_{1-x}, and Cu_xAu_{1-x} with compositions spanning $x = 0 \rightarrow 1$. The interior region of the triangle contains all possible $Cu_xAu_yPd_{1-x-y}$ compositions distributed like a ternary composition diagram. This library design is illustrated in the inset to Figure 2.

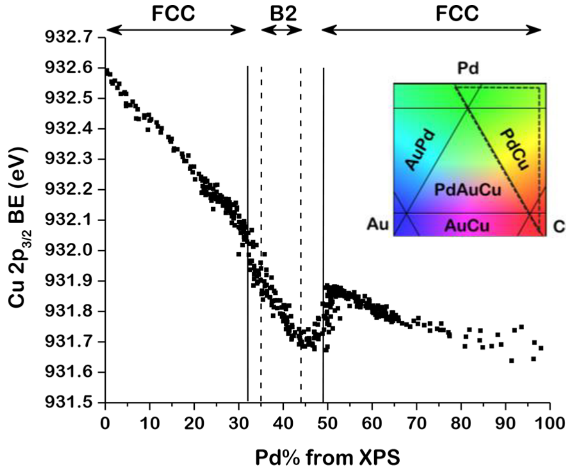

Figure 2. Cu 2p$_{3/2}$ core level binding energy in Cu_xPd_{1-x} as a function of Pd composition as measured on a $Cu_xAu_yPd_{1-x-y}$ CSAF. A graphic of the CSAF is shown in the inset with the Cu_xPd_{1-x} region bounded by the dashed line. The Cu 2p$_{3/2}$ core level decreases monotonically in energy in the regions with FCC structure. A discontinuity in the Cu 2p$_{3/2}$ core level binding energies is observed over the B2 phase composition range.

The $Cu_xAu_yPd_{1-x-y}$ CSAF is a 100 nm thick film deposited onto a 14 × 14 mm^2 Mo substrate by electron beam evaporation under UHV conditions. The rotating shadow-mask deposition tool used to prepare these CSAFs has been described elsewhere.[21,22] All three components were codeposited over an 8 h period to ensure perfect initial mixing. The substrate was held at room temperature during deposition but then annealed at 800 K for 1 h under UHV conditions. This annealing has been shown to be sufficient to generate the FCC and B2 phases in similar Cu_xPd_{1-x} CSAFs.[7,14,20]

The bulk composition of the $Cu_xAu_yPd_{1-x-y}$ CSAF has been mapped to physical location on the Mo substrate using energy dispersive X-ray (EDX) spectroscopy in a Tescan Vega3 LM SEM equipped with an Oxford Inca Energy 350 X-ray detector. EDX spectra were obtained from points on a 27 × 27 grid spaced at 0.5 mm. Spectra were obtained while rastering the 20 keV electron beam across a 50 × 50 μm^2 area of the CSAF, and the data were obtained using 80 s live time for acquisition at each point. The EDX spectra were analyzed using the ThinFilmID to determine the molar thickness of each component and thereby the film composition as a function of position across the CSAF.

2.2. XPS Mapping of Core Level Shifts. X-ray photoemission analysis of the CSAF was performed in a ThermoFisher ThetaProbe. The sample was mounted on a holder that allowed annealing to 1000 K. Within the ThetaProbe, the sample was moved by an automated stage allowing analysis of the CSAF surface at a set of predetermined points or CSAF compositions. XP spectra were obtained with the X-ray source focused to a spot on the surface at the focal point of the analyzer. Spatially resolved maps of the Cu $2p_{3/2}$, Au $4f_{7/2}$, and Pd $3d_{3/2}$ XP spectra were obtained by lateral translation of the CSAF such that its plane intersected the source-analyzer focal point. When mapping XP spectra with a 0.5 mm spot spacing, the X-ray spot was focused to 200 μm diameter. When mapping with a 0.1 mm spacing, it was focused to 100 μm diameter. Given that the spatial extent of the entire composition spread for each component of the CSAF is ~8 mm, the spread in composition under the 200 μm diameter X-ray spot was ~2.5%. XP spectra were obtained using snap mode with a pass energy of 40 eV and a total data collection time of 20 s (for all three elements) at any given point. The local composition at any point on the CSAF is reported in terms of the composition determined from the XPS peak intensities scaled using the adjusted Scofield sensitivity factors supplied by the manufacturer. The core level binding energies of each of the three components are reported by fitting the spectra using a Gaussian−Lorentzian function and finding the binding energy of its maximum.

2.3. He Ion Bombardment of the CuAuPd CSAF. He^+ ion bombardment of the CSAF surface was used both to clean the surface and to induce disorder. He^+ was chosen because of its large mass mismatch with the alloy components and, therefore, the low probability of sputtering metals from the surface. XPS showed that there was no measurable change in the near surface composition of the CSAF as a result of He^+ bombardment. The CSAF surface was cleaned by sputtering for 3 min per spot with a 1.15 nA beam of 1 kV He^+ ions focused to a spot with a diameter of ~500 μm. The cleanliness of the surface was determined by monitoring the C 1s XPS signal. The surface was then disordered by bombardment for 6 min per spot with a 4.4 μA beam of 1 kV He^+ ions.

3. RESULTS

3.1. Cu $2p_{3/2}$ CLS in Cu_xPd_{1-x}. Several studies of the Cu $2p_{3/2}$ and Pd $3d_{3/2}$ core level binding energies in Cu_xPd_{1-x} alloys have shown that they depend on the alloy composition, x.[18−20] The earliest measurements were made on a set of 21 discrete composition samples annealed at 1000 K to ensure that all were in their FCC phase.[19] Those measurements demonstrated that there is a continuous monotonic decrease in the Cu $2p_{3/2}$ binding energy as the alloy becomes increasingly dilute in Cu; i.e., x decreases. More recently, a binary Cu_xPd_{1-x} CSAF has been used to study the CLS in a film that was annealed at 800 K such that it exhibited the B2 phase for compositions in the range $0.50 < x < 0.65$.[7,20] These measurements revealed that, in addition to the smooth monotonic CLS associated with dilution, there is a discontinuous offset in the CLS over the composition range in which the B2 phase is found. Computational modeling of this phenomenon showed that it can be associated with the fact that Cu atoms are isolated from one another in the ordered B2 phase.[20]

The work reported herein has explored the core level shift in a ternary $Cu_xAu_yPd_{1-x-y}$ CSAF, as depicted schematically in the inset to Figure 2. XP spectra have been obtained at 487 points on the $Cu_xAu_yPd_{1-x-y}$ CSAF lying in the region outlined by the dashed triangle and having compositions with <1 at. % Au. This CSAF was annealed at 800 K for 1 h prior to XPS collection. Note that analysis using electron backscatter diffraction has confirmed the existence of the B2 phase in a 100 nm thick Cu_xPd_{1-x} binary CSAF annealed at 800 K. The increased scatter in the measured Cu $2p_{3/2}$ binding energies at high Pd concentrations arises from the fact that the Cu concentration becomes very low and the weak XPS signal hinders accurate measurement of the Cu $2p_{3/2}$ binding energy. The data in Figure 2 quantitatively reproduce those obtained from the Cu_xPd_{1-x} binary CSAF and clearly reveal the discontinuous behavior of the CLS in the composition range from $0.50 < x < 0.65$, exactly the region in which one expects to find the B2 phase and the two-phase regions that contain both the random FCC alloy and the B2 phase.

The Cu $2p_{3/2}$ CLS for the FCC phase alloy has a decreasing slope with respect to increasing Pd composition (Figure 2). This is noticeable in prior data sets but not commented on in prior work, perhaps because their much more limited data sets do not make this curvature so obvious.[18−20] The curvature of CLS versus Pd composition is consistent with prior computational modeling showing that the CLS is determined by the average number of Cu atoms in the nearest neighbor shell of the ionized Cu atom.[20] At high Cu concentrations, the extraction of each Cu atom reduces by one the number of Cu atoms in the nearest neighbor shells of the surrounding 12 Cu atoms. At very low Cu concentrations (high Pd), the Cu atoms are already isolated from one another and thus the removal of a Cu atom has a negligible impact on the nearest neighbor shells of the remaining Cu atoms. The average number of Cu atoms in a Cu nearest neighbor shell is nonlinear in Pd composition, and hence, the Cu $2p_{3/2}$ CLS in the FCC phase should be a nonlinear function of Pd composition.

3.2. CLS in CuPd, CuAu, and AuPd Binary Alloys. In order to determine the maximum Au composition, y, to which the B2 phase exists in the $Cu_xAu_yPd_{1-x-y}$ ternary alloy, the core level binding energies were measured for all three components across all compositions of the CSAF. These are plotted in Figure 3 for the Cu $2p_{3/2}$, Au $4f_{7/2}$, and Pd $3d_{3/2}$ levels relative to their values in the pure components. Note that the CLS are only reported for alloy compositions above 15 at.%, as they are not accurately determined once the alloy becomes dilute.

At 800 K, the binary AuCu and AuPd alloys form random solid solutions. In the binary alloys, the Au $4f_{7/2}$ CLS (lower left corner of Figure 3) exhibits the simplest behavior. During dilution to 15 at. % in Pd, there is a monotonic decrease in the Au $4f_{7/2}$ binding energy by −0.6 eV, whereas dilution of Au to 15 at. % in Cu results in a Au $4f_{7/2}$ CLS of +0.4 eV. In contrast, there are no detectable shifts in either the Cu $2p_{3/2}$ (upper panel of Figure 3) or Pd $3d_{3/2}$ (lower right panel of Figure 3) binding energies during their dilution to 15 at. % in Au.

The more interesting CLS behavior is revealed by the Cu $2p_{3/2}$ and Pd $3d_{3/2}$ binding energies in the CuPd binary. The Cu $2p_{3/2}$ binding energy shifts by −0.9 eV during dilution to 15 at. % in Pd. The Pd $3d_{3/2}$ core level shifts by +0.5 eV during dilution to 15 at. % in Cu. These shifts in opposite directions suggest that part of their origin is charge transfer between Cu and Pd, although the data for the CuAu and AuPd binaries indicate that the origins of these shifts arise from additional factors. In those cases, the Au $4f_{7/2}$ level shifts while the Cu $2p_{3/2}$ and Pd $3d_{3/2}$ levels do not. The CLS associated with the

DOI: 10.1021/acs.jpcb.7b06652
J. Phys. Chem. B 2018, 122, 764−769

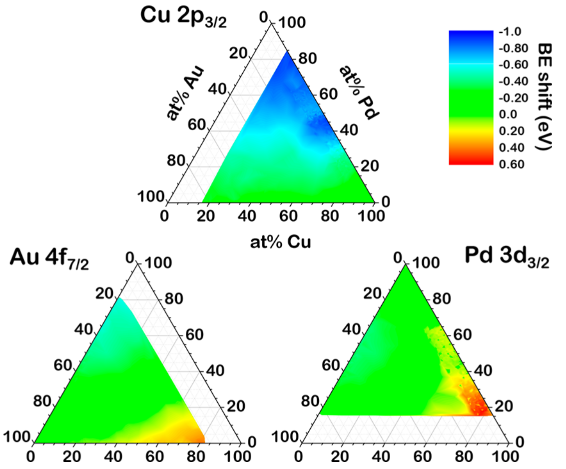

Figure 3. Cu $2p_{3/2}$, Au $4f_{7/2}$, and Pd $3d_{3/2}$ core level binding energies in $Cu_xAu_yPd_{1-x-y}$ relative to their values in the pure components. The Cu $2p_{3/2}$ level exhibits the greatest shift when diluted in Pd. The CLS discontinuity is visible in the composition region 33−55 at. % Pd and extends to ∼20 at. % Au. XP spectra were obtained with 40 eV pass energy and using 20 s of data collection for each element at each point.

phase transition in the CuPd binary is identifiable in the top panel of Figure 3 as the semicircular region of negative shift (blue) with a perimeter intersecting the Pd axis at 35 and 55 at. %. As mentioned earlier, electronic structure calculations have shown that this discontinuous CLS is the result of the transition from a FCC solid solution in which the Cu atoms are randomly distributed to the B2 structure in which they are isolated and, therefore, have no Cu atoms in their nearest neighbor shell.[20]

3.3. CLS in $Cu_xAu_yPd_{1-x-y}$. The CLS data in Figure 3 reveal the extent of the B2 alloy phase in the Au-containing region of the ternary alloy. This is more clearly revealed in Figure 4A, which plots the Cu $2p_{3/2}$ CLS across the ternary space with >15 Cu at. % and using a different CLS color scale. Figure 4A also plots the position of the B2 (and B2 + FCC two-phase region) relative to the discontinuity in the Cu $2p_{3/2}$ CLS. The coincidence of the two regions is clear.

In order to provide further evidence demonstrating that the discontinuous Cu $2p_{3/2}$ CLS arises from the change in phase from FCC to B2, we have purposefully disordered the near surface region of the CSAF by sputtering with a 4.4 μA beam of 1 keV He^+ ions for 6 min per spot. This is sufficient to induce disorder in the surface without causing any significant changes in the local composition of the sample as measured using XPS. The disorder is revealed by the CLS, as depicted in Figure 4B. The CLS is now a smooth, continuous function of composition across the entire composition space. Presumably, in what had been the ordered B2 region, Cu atoms are now in a metastable random solid solution phase in which they have Cu nearest neighbors in concentrations that are smooth functions of composition. Finally, one can explore the stability of this phase by annealing and then using the CLS to observe the reformation of the B2 phase. Figure 4C shows the CLS versus alloy composition in the CuPd binary region following annealing at temperatures in the range 300−800 K. Immediately after He^+ sputtering at 300 K, the CLS is a smooth function of composition, showing no evidence of the discontinuity asssociated with the B2 phase. Annealing at 500 K is sufficient to nucleate the formation of some B2 phase, whereas annealing at 600 K is sufficient to fully restore the B2 phase to its state immediately after deposition and annealing at 800 K.

Finally, we examine the accuracy with which the extent of the B2 phase can be mapped using the Cu $2p_{3/2}$ CLS. The left-hand panel of Figure 5 shows the CLS plotted over a narrow range of ternary alloy compositions. The black points are the locations in composition space of the points at which XP spectra were obtained. A quadratic background was fit to the spectral intensity outside the region containing the B2 and B2 + FCC phases: $E_{\text{bkg}}^{\text{CLS}}(x, y) = -3.3 \times 10^{-2} - 7.2 \times 10^{-3}x - 1.5 \times 10^{-2}y + 2.2 \times 10^{-5}xy + 7.5 \times 10^{-5}x^{2} + 6.4 \times 10^{-5}y^{2}$. This smooth background was then subtracted from the CLS map to yield Figure 5 (right) which highlights the extent of the B2 phase across the ternary composition space. It appears to extend to roughly 20 at. % Au which is fairly consistent with the established phase diagram.

4. DISCUSSION

We have assigned the discontinuous Cu $2p_{3/2}$ CLS observed in Cu_xPd_{1-x} and $Cu_xAu_yPd_{1-x-y}$ alloys to the presence of the B2 phase. Prior work has suggested that the CLS discontinuity arises from isolation of Cu atoms from one another in the ordered B2 phase.[20] Our assignment of the observed

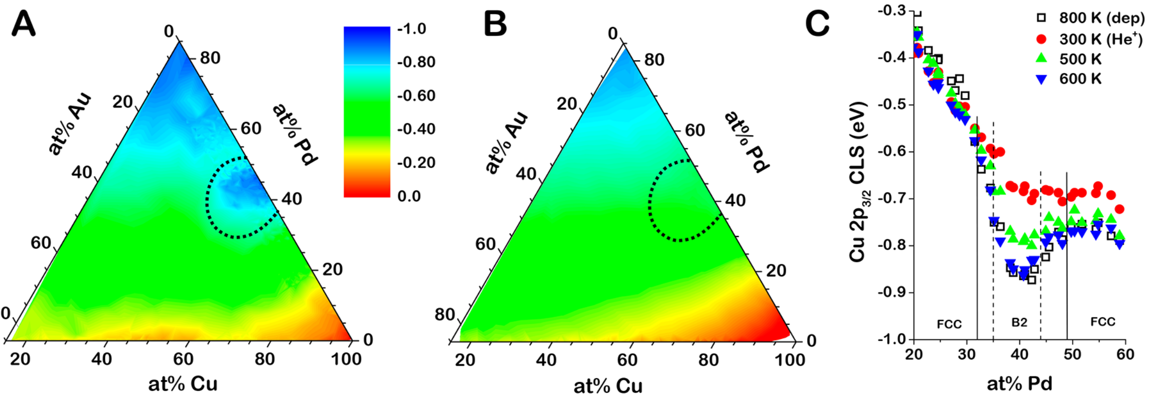

Figure 4. (A) Cu $2p_{3/2}$ CLS versus $Cu_xAu_yPd_{1-x-y}$ composition. The dashed line encloses the region containing the B2 and the two-phase (B2 + FCC) region reported from the phase diagram.[17] (B) The CLS after ion bombardment with 1 keV He^+ for 1 h. The CLS discontinuity associated with the B2 phase is absent, indicating the presence of a random distribution of Cu. (C) Plots of the CLS versus Pd at. % along the CuPd binary composition line. Annealing restores the B2 phase, which is completely reformed by 600 K.

DOI: 10.1021/acs.jpcb.7b06652
J. Phys. Chem. B 2018, 122, 764−769

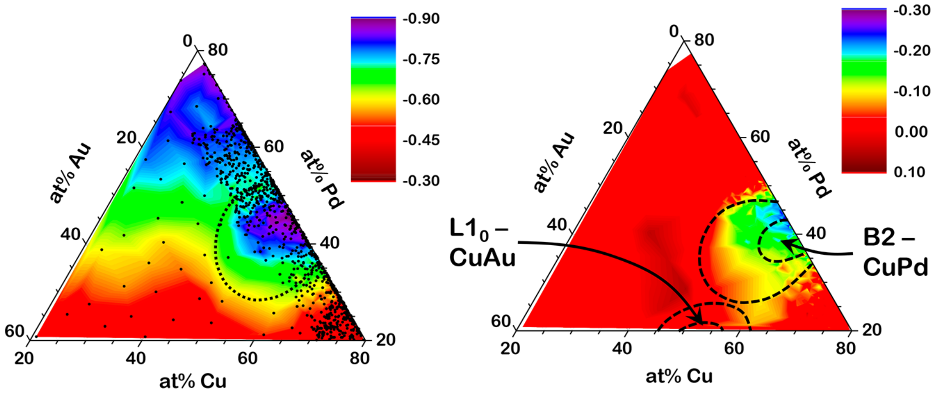

Figure 5. (left) The Cu $2p_{3/2}$ CLS map across a limited region of the ternary $Cu_xAu_yPd_{1-x-y}$ composition space. The black dots indicate the compositions at which XP spectra were obtained. The region outside the dashed curve was used to define a smooth quadratic background. (right) Background subtracted CLS revealing the discontinuous region around the B2 phase with high contrast. The boundaries of the B2, $L1_0$, and their surrounding two-phase regions are marked with the dashed curves.

discontinuity to this B2 phase is supported by three observations:

(1) The coincidence of the physical extent of the CLS across composition space and the known extent of the B2 and B2 + FCC regions.

(2) The fact that physical disordering of the $Cu_xAu_yPd_{1-x-y}$ by He^+ sputtering results in the disappearance of the CLS and that annealing restores it.

(3) There is no corresponding CLS in the region of the composition space that ought to exhibit the $L1_0$ phase which does not structurally isolate Cu atoms from one another.

The ability to detect phases on the basis of XPS CLS in the $Cu_xAu_yPd_{1-x-y}$ alloy suggests that the method can be used in other alloy systems that exhibit the same characteristics of phase transitions that result in changes in the local distribution of atoms and their nearest neighbors. Examples include AlNi and AlCo. Perhaps more importantly, the ability to detect phase transitions using CLS offers the opportunity to use XPS as a means of distinguishing phases in material morphologies such as nanoparticles and thin films for which diffraction methods might not be amenable.

Finally, the work presented herein illustrates the value and potential of CSAFs as high throughput libraries for the study of problems in materials and surface science. To begin with, the discovery of the Cu $2p_{3/2}$ CLS discontinuity associated with the B2 phase had not been made before our study of this system using CSAFs.[20] Equally importantly, the data set collected in this work would not have been possible using single composition alloy samples simply because of the time and effort needed to prepare them individually and for collection of XP spectra from each sample. Furthermore, the quality of the data and the ability to measure XP CLSs with the accuracy demonstrated using single CSAF libraries would not be possible with conventional methods.

5. CONCLUSIONS

Mapping of core level binding energy shifts across CSAFs serves as a high throughput method for mapping alloy phase diagrams, provided that the phase boundaries exhibit structural transitions that induce discontinuous core level shifts. This has been demonstrated for the FCC–B2 phase boundaries in $Cu_xAu_yPd_{1-x-y}$. The FCC–B2 phase transition exhibits a discontinuous CLS because the local distribution of Cu atoms changes from random to ordered across the phase boundary.

■ AUTHOR INFORMATION

Corresponding Author

*E-mail: gellman@cmu.edu. Phone: 1-412-268-3848.

ORCID

Andrew J. Gellman: 0000-0001-6618-7427

Notes

The authors declare no competing financial interest.

■ ACKNOWLEDGMENTS

The work reported herein has been supported by the US National Science Foundation under Grant No. CHE-1704871.

■ REFERENCES

(1) Bajaj, S.; Haverty, M. G.; Arroyave, R.; Goddard, W. A.; Shankar, S. Phase Stability in Nanoscale Material Systems: Extension from Bulk Phase Diagrams. *Nanoscale* **2015**, *7*, 9868–9877.

(2) Kusada, K.; Kitagawa, H. A Route for Phase Control in Metal Nanoparticles: A Potential Strategy to Create Advanced Materials. *Adv. Mater.* **2016**, *28*, 1129–1142.

(3) Bondesgaard, M.; Mainakhel, A.; Becker, J.; Kasai, H.; Philippo, G.; Bremholm, M.; Iversen, B. B. Supercritical Flow Synthesis of $Pt_{1-x}Ru_x$ Nanoparticles: Comparative Phase Diagram Study of Nanostructure Versus Bulk. *Chem. Mater.* **2017**, *29*, 3265–3273.

(4) Zornoza, B.; Casado, C.; Navajas, A. Advances in Hydrogen Separation and Purification with Membrane Technology. *Renewable Hydrogen Technologies*; Elsevier Publ.: Amsterdam, 2013; pp 245–268.

(5) Yun, S.; Oyama, S. T. Correlations in Palladium Membranes for Hydrogen Separation: A Review. *J. Membr. Sci.* **2011**, *375*, 28–45.

(6) Nielsen, B. C.; Dogan, O. N.; Howard, B. H.; Nall, E. Comparison of the Corrosion of $Cu_{50}Pd_{50}$ and $Cu_{50}Pd_{44}M_6$ (M = Y, Mg, or Al) Hydrogen Separation Membrane Alloys in Simulated Syngas Containing H_2S. *Corros. Sci.* **2013**, *76*, 170–181.

(7) Miller, J. B.; Priyadarshini, D.; Gellman, A. J. Segregation at the Surfaces of Cu_xPd_{1-x} Alloys in the Presence of Adsorbed S. *Surf. Sci.* **2012**, *606*, 1520–1526.

(8) Kim, W. J.; Moon, S. H. Modified Pd Catalysts for the Selective Hydrogenation of Acetylene. *Catal. Today* **2012**, *185*, 2–16.

(9) Horold, S.; Vorlop, K. D.; Tacke, T.; Sell, M. Development of Catalysts for a Selective Nitrate and Nitrite Removal from Drinking Water. *Catal. Today* **1993**, *17*, 21–30.

DOI: 10.1021/acs.jpcb.7b06652
J. Phys. Chem. B 2018, 122, 764–769

(10) Anastasopoulos, A.; Hannah, L.; Hayden, B. E. High Throughput Optimisation of PdCu Alloy Electrocatalysts for the Reduction of Nitrate Ions. *J. Catal.* **2013**, *305*, 27−35.

(11) Reyes, P.; Figueroa, A.; Pecchi, G.; Fierro, J. L. G. Catalytic Combustion of Methane on Pd-Cu/SiO_2 Catalysts. *Catal. Today* **2000**, *62*, 209−217.

(12) Fernandez-Garcia, M.; Martinez-Arias, A.; Belver, C.; Anderson, J. A.; Conesa, J. C.; Soria, J. Behavior of Palladium-Copper Catalysts for CO and NO Elimination. *J. Catal.* **2000**, *190*, 387−395.

(13) Donato, M. G.; Ballone, P.; Giaquinta, P. V. Bain Transformation in Cu_xPd_{1-x} ($x \sim 0.5$) Alloys: An Embedded-Atom Study. *Phys. Rev. B: Condens. Matter Mater. Phys.* **2000**, *61*, 24−27.

(14) Priyadarshini, D.; Kondratyuk, P.; Picard, Y. N.; Morreale, B. D.; Gellman, A. J.; Miller, J. B. High-Throughput Characterization of Surface Segregation in Cu_xPd_{1-x} Alloys. *J. Phys. Chem. C* **2011**, *115*, 10155−10163.

(15) Kamakoti, P.; Morreale, B. D.; Ciocco, M. V.; Howard, B. H.; Killmeyer, R. P.; Cugini, A. V.; Sholl, D. S. Prediction of Hydrogen Flux through Sulfur-Tolerant Binary Alloy Membranes. *Science* **2005**, *307*, 569−573.

(16) O'Brien, C. P.; Miller, J. B.; Morreale, B. D.; Gellman, A. J. The Kinetics of H_2-D_2 Exchange over Pd, Cu, and PdCu Surfaces. *J. Phys. Chem. C* **2011**, *115*, 24221−24230.

(17) Bochvar, N.; Liberov, Y. *Au-Cu-Pd (Gold - Copper - Palladium): Datasheet from Landolt-Börnstein - Group IV Physical Chemistry · Vol. 11b: "Noble Metal Systems. Selected Systems from Ag-Al-Zn to Rh-Ru-Sc" in Springer materials*; Springer-Verlag: Berlin, Heidelberg.

(18) Olovsson, W.; Abrikosov, I. A.; Johansson, B. Core Level Shift in Random CuPd and AgPd Alloys by the Complete Screening Picture. *J. Electron Spectrosc. Relat. Phenom.* **2002**, *127*, 65−69.

(19) Martensson, N.; Nyholm, R.; Calen, H.; Hedman, J.; Johansson, B. Electron-Spectroscopic Studies of the Cu_xPd_{1-x} Alloy System - Chemical Shift Effects and Valence Electron Spectra. *Phys. Rev. B: Condens. Matter Mater. Phys.* **1981**, *24*, 1725−1738.

(20) Boes, J. R.; Kondratyuk, P.; Yin, C. R.; Miller, J. B.; Gellman, A. J.; Kitchin, J. R. Core Level Shifts in Cu-Pd Alloys as a Function of Bulk Composition and Structure. *Surf. Sci.* **2015**, *640*, 127−132.

(21) Fleutot, B.; Miller, J. B.; Gellman, A. J. Apparatus for Deposition of Composition Spread Alloy Films: The Rotatable Shadow Mask. *J. Vac. Sci. Technol., A* **2012**, *30*, 061511.

(22) Payne, M. A.; Miller, J. B.; Gellman, A. J. High-Throughput Characterization of Early Oxidation across $Al_xFe_yNi_{1-x-y}$ Composition Space. *Corros. Sci.* **2015**, *91*, 46−57.